Engineering Structures 294 (2023) 116742

Contents lists available at ScienceDirect

Engineering Structures

journal homepage: www.elsevier.com/locate/engstruct

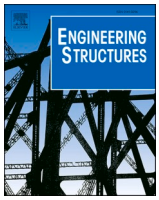

Design and production of an experimental UHPFRC bending-active footbridge

Carlos Lázaro [a,*], Carmen Castro-Bugallo [b], Juan Navarro-Gregori [b], Enrique Priego-de-los-Santos [c], Pedro Serna [b]

[a] Department of Continuum Mechanics and Theory of Structures, Universitat Politècnica de València, Camino de Vera s/n, 46022 Valencia, Spain
[b] ICITECH, Universitat Politècnica de València, Camino de Vera s/n, 46022 Valencia, Spain
[c] Department of Cartographic Engineering, Geodesy and Photogrammetry, Universitat Politècnica de València, Camino de Vera s/n, 46022 Valencia, Spain

ARTICLE INFO

Keywords:
Ultra-high performance fibre reinforced concrete (UHPFRC)
Active bending
Experimental footbridge

ABSTRACT

This paper describes the design, production and testing of an experimental footbridge made of ultra-high-performance fibre-reinforced concrete (UHPFRC). The prototype has a span length of 5.4 m and is made of a very slender pre-stressed UHPFRC deck (6 cm deep, 1.2 m wide), a 0.55 m high central deviator of the same material, and an external lower tensioning stainless-steel cable system. The service configuration of the structure involves a significant permanent bending of the deck, because of its slenderness; this initial bending is introduced in a controlled manner during the production process and prior to the installation, and results in an efficient, lightweight, and elegant structure with a high stiffness-to-self-weight ratio. The structural concept belongs to the category named *active bending*, which has been recent subject of research. Specifically, the structure is a bow-string system in which the bending-active member is made of UHPFRC, which constitutes the main novelty of this research. The suitability of UHPFRC as a material for bending active applications has been investigated, and a method to determine the limiting pre-stress of UHPFRC bending-active cross sections has been developed. The activation process and relevant limit states have been checked by means of a 3D frame finite-element model. The paper concludes with the description of the production process and the installation of the footbridge in the final location, as well as the successful results of the load tests and the geometric control of the novel footbridge prototype.

1. Introduction

Ultra-High-Performance Fibre-Reinforced Concrete (UHPFRC) is a type of concrete capable of reaching very high compressive strength: 120–200 MPa. It is reinforced with thin steel fibres that confer ductility and a high tensile strength ranging from 7 to 12 MPa. Compared to conventional and high-strength concretes, UHPFRC allows to shape structural elements with considerable material savings, which benefits sustainability [1]. These properties make possible to design remarkably slender structural members with less passive reinforcement [2] that lead to designs in which the proportions of structural members are in the interface between conventional structural concrete sections and steel profiles. The possibility to design with such slender elements opens the way to explore novel lightweight structural concepts using UHPFRC members.

Designing buildings and structures with very slender members has been customarily avoided because it is usually associated with insufficient stiffness and, in some cases, with the risk of buckling. However, in the last decades, this paradigm has changed: inspired in traditional dwellings made of flexible laths (as *yurts*) and boosted by the availability of high-performance materials, several structures where structural members have been intentionally bent in order to achieve a curved structural shape have been designed and built. Two remarkable examples are the pioneering *Multihalle Mannheim* [3] and more recently the ephemeral cathedral of Créteil (Paris) [4]. In both cases a kinetic grid of continuous slender structural members has been assembled on the ground and lifted to a curved geometry. The lifting process induces large deformations of the grid caused by bending of every individual bar. Once the planned geometry is achieved, bars are fixed to ground supports and stabilized by means of additional members or cables. The result is an elastically deformed, dome-shaped grid – called *elastic gridshell* in the literature – with remarkable stiffness (as a result of the

* Corresponding author.
E-mail address: carlafer@mes.upv.es (C. Lázaro).

https://doi.org/10.1016/j.engstruct.2023.116742

Available online 15 August 2023

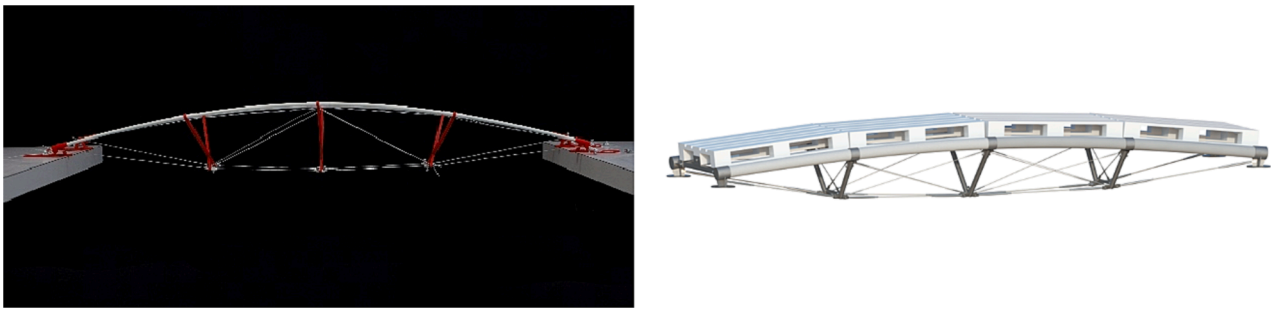

Fig. 1. Concept (left) and design (right) of a bending-active GFRP footbridge. Source: [7]

imposed curved spatial shape) and lightness. The Mannheim structure is made of timber laths and the Créteil dome is made of GFRP tubes; in both cases, the structural concept takes advantage of the large ratio between flexural strength and Young's modulus of timber and GFRP; this is a requirement to ensure a safe behaviour when large curvatures have been intentionally induced and are kept throughout the service life of the structure. The strategy of using elastic bending deformation of slender structural members to achieve a desired structural shape is called *active bending*; it has been a subject of research and experimentation in recent years [5].

Several advantages of bending-active structures compared to other lightweight structural types can be mentioned: very low material consumption, simple production of structural elements because of their straight shape, and rapid assembly. In contrast, they require a more complex design and erection process due to the large structural deformations occurring at that stage; in addition, initial bending consumes a relevant part of the flexural strength of the material and may cause creep of the material. However, the limited availability of resources and the need to reduce carbon footprint lead to investigating the feasibility of lightweight structural types with reduced material consumption, and bending-active structures fall within this category. Whereas most experimental bending-active structures are small-scale lightweight pavilions and domes, the application of active bending to footbridges was limited until recently to an experimental structure made of two GFRP pultruded slabs glued together in a pre-bent configuration [6]; it is therefore a rather unexplored field. In previous works, our group has studied the possibilities of using active bending to shape lightweight footbridges composed of flexible GFRP tubes, deviators and cables, and proposed procedures to systematise their design. A summary of the relevant aspects of our previous research on bending-active bow-string arches follows. The concept of a bending-active lightweight footbridge with GFRP bent members for the deck, deviating struts and tensioning cables was proposed in Ref. [7] (Fig. 1). Ref. [8] investigates the design parameters, the structural performance and the ultimate limit states of this type of bending-active bow-string arches. More specifically, the relationship between the activation forces in the external cables, the mechanical properties of the bent elements and the geometric proportions of the structure on the one hand, and the influence on the design parameters in the ultimate and serviceability limit states, on the other hand, were thoroughly analysed. Finally, Ref. [9] proposes a multi-objective optimisation algorithm to adjust the design parameters leading to performant bending-active tied arches. The experimental UHPFRC footbridge in this article is based on a simpler version of the structural concept object of the mentioned references.

Kotelnikova-Weiler *et al.* [10] developed a thorough study of suitable materials for active-bending applications based on Ashby's methodology [11]. According to it, the following material requirements are needed: high elastic limit strain; high material stiffness; high tenacity; low price for a given performance; high environmental properties and high durability. Their conclusion is that fibre reinforced polymers, as well as oak and fir wood are the best suited materials for active bending, mainly due to their combination of high strength and rigidity. Although at first sight UHPFRC does not seem to fit into the class of materials suitable to undergo large flexural deflections, the concept of bending concrete is not a new one: Dante Bini introduced a method to build domes in the 1960s by casting the mixture on a membrane, and subsequently inflating it before the concrete has set [12]. More recently, Kromoser and Kolleger [13] developed a variant of Bini's method by casting thin flat panels of textile reinforced concrete and bending them into a 3D shape by means of an inflatable membrane once the concrete has hardened. The resulting domes show a smeared cracking pattern in the target curved shape. This approach is close to active bending, the main difference being the fact that the material cracks and is not working elastically during activation. A similar idea was used by Ochs *et al.* [14] for the construction of roof elements using a sandwich of very thin pre-deformed UHPFRC plates with PUR core to form a barrel vault. To the authors' knowledge, there are no other examples of use of UHPFRC in bending-active applications. However, UHPFRC brings together many of the material requirements listed by Kotelnikova-Weiler *et al.* in [10]: it has a remarkable compressive-strength-to-stiffness ratio, it is a rather tough and ductile material, it is durable, has low creep and lightweight applications make it cost-competitive. It must be mentioned that a substantial difference between UHPFRC and GFRP or timber is the fact that its tensile strength is much lower than the compressive one; this is disadvantageous in pure bending applications because the flexural strength is limited by the tensile behaviour. However, this drawback is compensated by UHPFRC's significant residual tensile strength and ductility, its capacity to distribute cracking across regions working in tension thanks to the activation of the steel fibres once the matrix cracks, as well as the possibility to partially compensate for the lack of symmetry in the uniaxial behaviour through prestressing.

Building upon our experience in the design of lightweight bending-active structures ([7,8,9]), in the application of UHPFRC to the design and construction of real-scale footbridges [2], and in the serviceability behaviour of UHPFRC [15], we investigate the suitability of UHPFRC to be applied in lightweight structures where structural elements are pre-bent to reach the desired structural shape. The purpose of our research is twofold: on one hand, to analyse the feasibility of UHPFRC to be used as material for bending-active structural elements; on the other hand, to explore the possibility to build UHPFRC lightweight footbridges using the bending-active concept through the design and production of a small prototype that serves as proof-of-concept. It has been built using a UHPFRC on the boundary between the strain hardening and softening in tension. The lower fibre content, compared to the required for UHPFRC with strain hardening, leads to a competitive structural solution while keeping the necessary performance. Preliminary findings in this investigation have been published in a conference paper [16]; this article substantially expands the information therein, including the theoretical results, as well as the details and assessment of the production and the test results.

The article is organized as follows. Section 2 analyses the flexural behaviour up to the failure of prestressed UHPFRC cross-sections to be

activated by bending. This part is crucial to assess the safety of the deck during the activation phase. Furthermore, a procedure is established to determine the limiting prestressing force to achieve maximum sectional performance. Section 3 describes the design of the experimental bow-string footbridge composed of an UHPFRC bending-active deck and a lower cable system that informs the shape of the deck and provides the necessary stiffness and strength to the structure. Section 4 shows the production process of the experimental footbridge and discusses some associated problems. The results of the loading tests, as well as the analysis of the results of a laser scan of the structure to survey its geometry are described in Section 5. Lastly, conclusions are discussed in Section 6.

2. Sectional behaviour of slender prestressed UHPFRC members

According to Russell and Graybeal [17], relevant values for the mechanical properties of UHPFRC are in the following ranges: compressive strength f_c=140 to 200 MPa; tensile strength f_{ct}=6 to 10 MPa; modulus of elasticity E=40 to 70 GPa; Poisson's ratio ν=0.2; thermal expansion ratio 10 to 15×10^{-6} °C^{-1}; total shrinkage up to 900×10^{-6}; specific creep 6 to 45×10^{-6} MPa^{-1}. In compression, UHPFRC shows a practically linear behaviour up to 70% to 80% of the compressive strength. Failure of specimens with no fibres has an explosive nature; however, a descending branch can be found when using steel fibres. In tension, the behaviour is linear until cracking appears; the material has a remarkable residual strength. The value of the tensile strength can be adopted as the elastic limit in tension. Creep is much less than in conventional concrete. At first sight, it could seem that the elastic range of UHPFRC in tension is too limited to be pre-deformed with significant curvature. However, the fact that fibres increase their efficiency after the onset of cracking until fibre pull-out starts [20], as well as the introduction of pre-stress, can compensate this asymmetrical behaviour.

The requirements for suitable materials in bending-active applications reflected in [10] have been usually defined by means of indexes. Two of them are related to the mechanical properties: the first one is the ratio flexural-strength-to-Young's-modulus; the second one is Young's modulus itself. These ratios play a key role, because materials with high values of both indexes are strong and flexible enough to work in a curved configuration, as well as safe enough against buckling. Lienhard [18] has proposed the following minimum ratio between the flexural strength and the modulus of elasticity for a material to be suitable for active bending: σ_{el} / E=2.5×10^{-3}. The ratio is related to the curvature that a rod of a given material can attain while remaining in the elastic range. Some metals (aluminium, titanium, and high-strength steels), carbon fibre and glass fibre composites, as well as some types of timber comply with Lienhard's criterion: as mentioned in the introduction, most examples of active bending are made of glass fibre composites or timber. Therefore, the given value for the ratio, rather than being a strict limit, reflects the properties of these materials. In the case of UHPFRC, the ratio between the proportionality limit stress in compression and the modulus of elasticity is in the range 2.3 to 2.8×10^{-3} according to the values given in [17]. However, such a ratio can't be attained by its tensile strength. In UHPFRC cross-sections, the possibility to reach larger curvatures is provided by the ductility of the material; therefore, the ratio involving the tensile strength should not be used as a limiting parameter when aiming at bending-active applications.

The purpose of this section is twofold: on one hand, to define a procedure to determine the moment–curvature relation for prestressed UHPFRC cross-sections, aimed at the design of bending-active applications; on the other, to show that in slender cross-sections, significant curvatures can be reached while keeping the equivalent UHPFRC strains under 0.002. For this strain value, fibres provide the maximum efficiency, and the UHPFRC tensile stress has a maximum value in the material model that we have implemented. Previous studies of our group [15] show that structural members subjected to traction have smeared micro-cracking up to yielding of reinforcement. Therefore, no localized cracking is expected for the mentioned strain level. Moreover, introducing higher prestress forces allows reaching larger section curvatures and provides substantial increases in the resisted bending moment. Passive reinforcement has not been considered in the analysis, because of the strict section depth associated to the active bending concept.

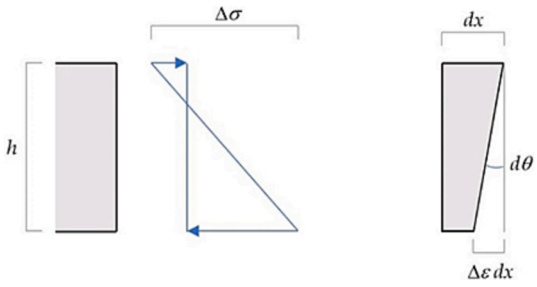

Fig. 2. Stress range and curvature in a cross-section [16].

2.1. Limit curvature from simplifying assumptions

To obtain a preliminary estimation of the imposed curvature that UHPFRC beams can safely undergo, a linear material behaviour is considered. The elastic relation between the unit rotation and the stress distribution in a beam of section depth h is given by (see Fig. 2) $d\theta/dx=\Delta\sigma/(E\,h)$. For shallow cross-sections, the shear deformation can be neglected, and the preceding formula is a fair approximation of the curvature χ of a structural element in terms of the stress range, the cross-section depth and Young's modulus.

A typical UHPFRC with elastic modulus E=50000 MPa, ultimate tensile strength $f_{\bar{u}}^{+}\approx$10 MPa, and ultimate compressive strength $f_{\bar{u}}^{-}\approx$150 MPa is considered here. In this preliminary analysis, the stress range in the activation stage can be limited to 50% of the difference between ultimate strength values, which means an allowable stress range $\Delta\sigma$ of 80 MPa. Note that the way in which prestress is introduced to balance tensile and compressive stresses is not analysed at this point. With these values, the approximate limiting relation between curvature and cross-section depth becomes:

$$\chi < 1.6\times10^{-3}/h \tag{1}$$

which in terms of the radius of curvature is equivalent to $R>625h$. This equation provides a first order of magnitude of the curvatures that can be achieved in the activation stage of a bending-active structure *while keeping sectional pseudo-elastic behaviour*. In the next subsections, a deeper analysis is carried out considering more accurate material properties and the effect of prestress.

2.2. Material properties for the analysis

The uniaxial model of UHPFRC in compression is taken from Annex 2 of Ref. [19]. The following relevant parameters to define the uniaxial stress–strain diagram have been considered: mean compressive stress f_{cm}=150 MPa, and mean deformation modulus E_{cm}=50000 MPa. With these data, the following characteristic strain values have been calculated: strain corresponding to the peak compressive stress considering confinement $\varepsilon_{c1,f}=-3.79\times10^{-3}$; ultimate strain corresponding to $0.7f_{cm}$ in the descending branch considering confinement $\varepsilon_{c2,f}=-6.15\times10^{-3}$. For the uniaxial tensile behaviour, a mean post-cracking tensile strength f_{ctfm}=7 MPa has been assumed. The corresponding strain is $\varepsilon_{ct1}=f_{ctfm}/E_{cm}=0.14\times10^{-3}$. According to Leutbecher and Fehling [20], fibre efficiency increases after the initiation of cracking up to a maximum. Once it is reached, fibre pull-out starts, and the efficiency decreases for larger crack width. In our uniaxial model, this is taken into account considering that UHPFRC stresses increase up to f_{ctfm}+1 MPa for an equivalent strain $\varepsilon_{ct2}=2\times10^{-3}$, which marks the maximum fibre efficiency, and after it,

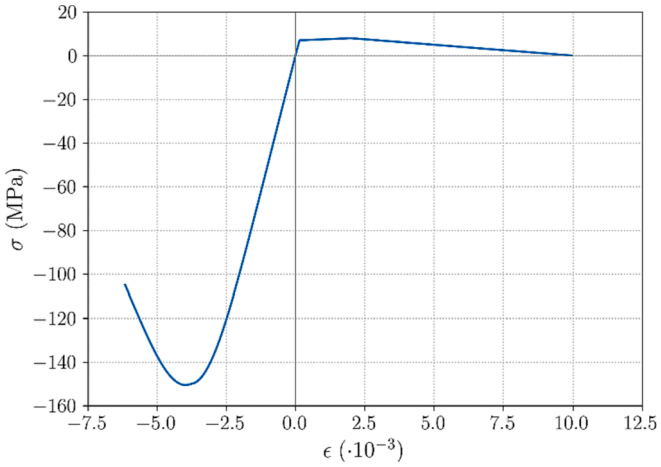

Fig. 3. Uniaxial stress–strain diagram for UHPFRC with f_{cm}=150 MPa, E_{cm}=50000 MPa and f_{ctfm}=7 MPa. Tensile stresses have positive values.

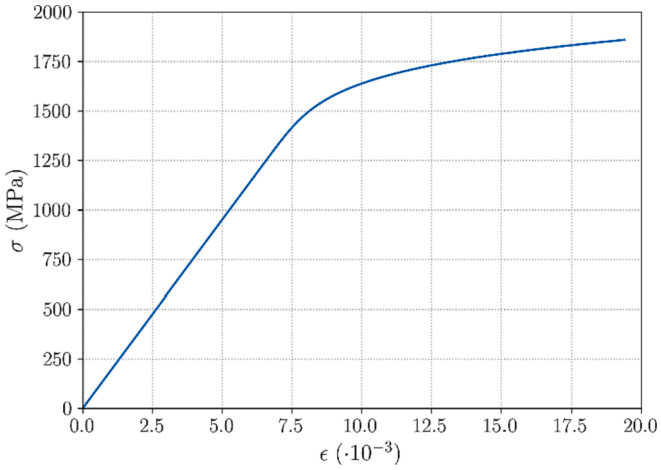

Fig. 4. Uniaxial stress–strain diagram for Y1860 prestressing steel strands.

stresses decrease to null for an ultimate tensile strain ε_{ct3}=10×10^{-3}. The complete stress–strain diagram is shown in Fig. 3.

The representative values for all material parameters from which the uniaxial model is derived have been defined based on our group's experience working with this type of UHPFRC. In particular, the values defining the representative tensile behaviour and the methodology to obtain them from laboratory tests, are discussed in Ref. [1].

The uniaxial stress–strain model for the prestressing steel diagram included in the Spanish EHE-08 code [22] has been adopted, as it provides a better representation of the material behaviour than the design diagram of the Eurocode 2. For Y1860 steel strands, the ultimate strength is $f_{p,\max,k}$=1860 MPa, and the characteristic strength is f_{pk}=0.9$f_{p,\max,k}$=1674 MPa. The diagram is linear with elasticity modulus E_p=190000 MPa for stress values σ_p under 70% of the characteristic tensile strength f_{pk} and has the following polynomic expression for larger stresses up to $f_{p,\max,k}$: ε_p=σ_p/E_p+0.823(σ_p/f_{pk}–0.7)^5. The resulting diagram is represented in Fig. 4.

2.3. Moment-curvature diagrams

Much more accurate values of the limiting curvatures of UHPFRC cross-sections than those of Section 2.1 can be obtained performing sectional analysis with the material properties presented in the previous section. With this purpose, the sectional behaviour of a slender rectangular UHPFRC cross-section 100 mm (width) × 50 mm (depth) under

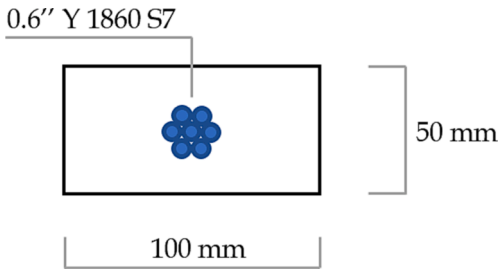

Fig. 5. Typical cross-section to study moment–curvature diagrams.

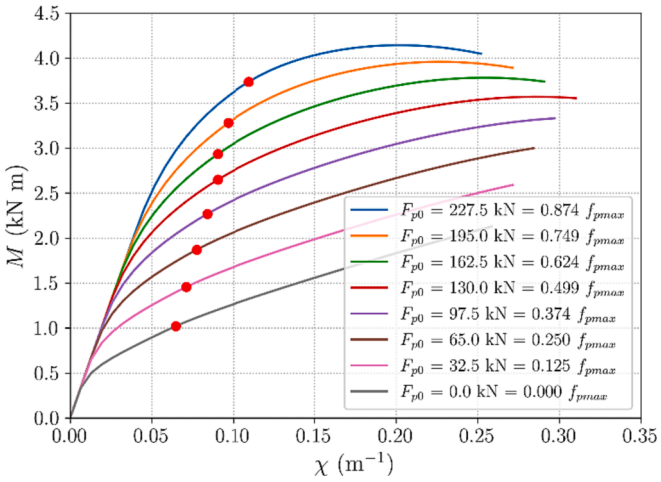

Fig. 6. Moment-curvature diagrams of a 100 mm × 50 mm rectangular UHPFRC cross-section for different values of the prestressing force. Red dots correspond to a 0.002 tensile strain in UHPFRC. (For interpretation of the references to colour in this figure legend, the reader is referred to the web version of this article.)

different pre-stressing forces introduced by means of a single centred 0.6″ Y1860 S7 post-tensioning strand with $f_{p,\max,k}$=1860 MPa has been studied (see Fig. 5).

Moment-curvature diagrams are generated for different values of the prestressing force ranging from 0 to 227.5 kN (87.4% of $f_{p,\max,k}$). A standard procedure based on the plane section assumption, prescribing sectional equilibrium, and considering the UHPFRC stress–strain

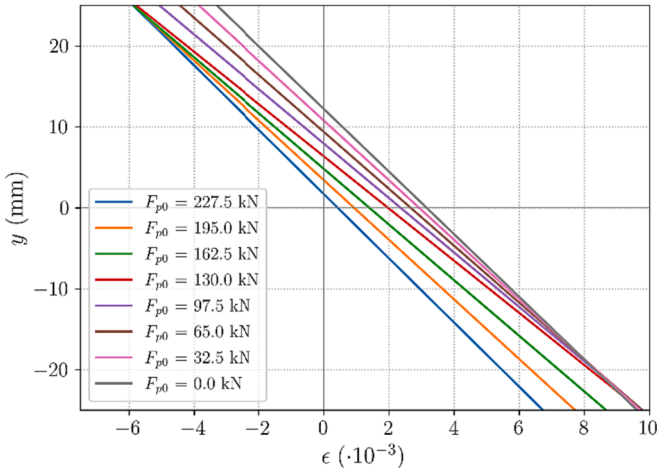

Fig. 7. Ultimate uniaxial strain distribution on the UHPFRC along the depth of a 100 mm × 50 mm rectangular cross-section for different values of the prestressing force. Elongations have positive values.

diagram (Fig. 3) and the Y1860 stress–strain diagram (Fig. 4), has been implemented using Python code. For each value of the curvature between an initial one after transferring prestress and a final one corresponding to the limiting compressive and tensile strains at the top/bottom fibres, the algorithm iterates until equilibrium of axial forces in the cross-section is reached, solving for the UHPFRC strain at the level of the centroid, and calculating the bending moment from the solution.

Fig. 6 shows the resulting moment–curvature diagrams. The red dot on each curve shows the situation corresponding to an equivalent UHPFRC tensile strain $\varepsilon_{ct2}=2\times10^{-3}$. As explained in Section 2.2, for this strain value, fibres provide the maximum efficiency and the UHPFRC tensile stress reaches a maximum value in the uniaxial model. The end of each curve corresponds to the limit situation beyond no equilibrium is found for a small curvature increment. As expected, higher prestressing forces lead to higher ultimate bending moments. For this cross-section, a prestressing force corresponding to 50% of $f_{p,\max,k}$ (red curve) results in the largest achievable curvature. For higher prestressing forces the maximum bending moment is larger than the ultimate one.

Fig. 7 represents the UHPFRC uniaxial strain distribution corresponding to the ultimate curvature for each value of the prestressing force. The diagrams show that, in this cross-section, failure occurs when approximately reaching the ultimate tensile strain of UHPFRC ($\varepsilon_{ct3}=10\times10^{-3}$) for prestressing forces below 50% of $f_{p,\max,k}$, while for prestressing forces above this value, the cross section fails when reaching the ultimate compressive strain of UHPFRC ($\varepsilon_{c2,f}=-6.15\times10^{-3}$). The red line, corresponding to a prestress of $0.5f_{p,\max,k}$ marks the limiting case in which both ultimate compressive and tensile strains are reached simultaneously, and the maximum ultimate curvature is achieved.

The limit prestressing force corresponding to maximum curvature can be estimated for a general rectangular cross-section with dimensions $b\times h$ and a centred prestressing strand with area A_p by means of direct sectional analysis. Considering that at the ultimate state, UHPFRC strains reach the compressive and tensile limits at the top and bottom fibres, the strain of the centred prestressing strand is $\varepsilon_p=\varepsilon_{p0}+\varepsilon_{cg}$, with $\varepsilon_{cg}=(\varepsilon_{ct3}+\varepsilon_{c2,f})/2$, and the UHPFRC strain along the depth of the cross section is given by

$$\varepsilon_c(y)=\varepsilon_{cg}-(\varepsilon_{ct3}-\varepsilon_{c2,f})\frac{y}{h} \tag{2}$$

Assuming that the stresses in the prestressing strand still fall into the linear part of the stress–strain diagram, equilibrium of forces at the section level requires

$$E_pA_p(\varepsilon_{p0}+\varepsilon_{cg})+\int_{-h/2}^{h/2}\sigma_c(y)b\mathrm{d}y=0 \tag{3}$$

Once the stress–strain diagram is given, the stress resultant on the UHPFRC *has a constant value* provided that the limit strains are reached at the top and bottom fibres. This is easily shown by means of a change of variable in the integral:

$$\int_{-h/2}^{h/2}\sigma_c(y)b\mathrm{d}y=\int_{\varepsilon_{ct3}}^{\varepsilon_{cf2}}\sigma_c(\varepsilon_c)b\frac{\mathrm{d}y}{\mathrm{d}\varepsilon_c}\mathrm{d}\varepsilon_c \tag{4}$$

The derivative is calculated from Eq. (2). Plugging it in the integrand and swapping the integration limits yields

$$\int_{-h/2}^{h/2}\sigma_c(y)b\mathrm{d}y=\frac{bh}{(\varepsilon_{ct3}-\varepsilon_{c2,f})}\int_{\varepsilon_{c2,f}}^{\varepsilon_{ct3}}\sigma_c(\varepsilon_c)\mathrm{d}\varepsilon_c \tag{5}$$

The new integral is the (signed) area under the stress–strain curve between both limiting strains. Note that, for the sake of simplicity, the strand area has not yet been discounted. Let's define the *average UHPFRC stress at failure* as:

$$\overline{\sigma}_{cu}=\frac{1}{(\varepsilon_{ct3}-\varepsilon_{c2,f})}\int_{\varepsilon_{c2,f}}^{\varepsilon_{ct3}}\sigma_c(\varepsilon_c)\mathrm{d}\varepsilon_c \tag{6}$$

Using this definition and Eq. (3), the *limit prestressing force* for any rectangular cross section with centred prestress is given by

$$F_{p0}=E_pA_p\varepsilon_{p0}=-(bh\overline{\sigma}_{cu}+E_pA_p\varepsilon_{cg}) \tag{7}$$

This expression overestimates the prestressing force, because the UHPFRC stress distribution does not act on the whole gross area $A=bh$. A more accurate estimate is achieved when, instead of using the gross area, the net UHPFRC area A_c is used:

$$F_{p0}=E_pA_p\varepsilon_{p0}=-(A_c\overline{\sigma}_{cu}+E_pA_p\varepsilon_{cg}) \tag{8}$$

Note that the validity of this estimate depends on the fact that UHPFRC stresses are very low at the level of the prestressing strand. For the UHPFRC material parameters given in Sect. 2.2, the average UHPFRC stress at failure is $\overline{\sigma}_{cu}=-37.52$ MPa, and the estimate of the limiting prestressing force given by Eq. (8) for the cross-section of Fig. 5 is $F_{p0}=131.2$ kN, which matches the previously computed value (see Fig. 6, red curve).

2.4. Discussion

The results in the preceding section allow to draw several conclusions for the design of very slender prestressed UHPFRC cross-sections aimed at bending-active applications:

For a given cross section, there is a limit value for the prestressing force beyond which the failure of the cross section will be governed by the UHPFRC ultimate compressive strain in bending. This value corresponds to simultaneously reaching the UHPFRC tensile and compressive ultimate strains at the top and bottom fibres and defines a limiting curvature equal to

$$\chi_{lim}=\frac{\varepsilon_{ct3}-\varepsilon_{cf2}}{h}\approx\frac{16\times10^{-3}}{h} \tag{9}$$

which is 10 times larger than the initially estimated limiting curvature –Eq. (1)–; i.e., Eq. (9) represents the maximum curvature allowed by the behaviour of UHPFRC at the onset of failure, whereas the curvature in Eq. (1) was estimated assuming that the behaviour of UHPFRC was still within the elastic range.

The limiting prestressing force for a rectangular cross-section can be estimated using Eq. (8); lower values of the prestressing force will lead to ductile failures of the cross-section, albeit with lower ultimate moments and lower values of the curvature at failure. For sections with different shapes, sectional analysis using the algorithm presented in Sect. 2.3 is required to determine the limiting prestressing force.

Red dots in Fig. 6 mark moment–curvature pairs for which the tensile strain in UHPFRC is equal to 0.002, which corresponds to the peak value of the UHPFRC tensile strain. Focusing on these moment–curvature pairs, it is remarkable that increasing the prestress force in the cross-section produces steady, quasi-linear increases of both, the bending moment and the curvature. Even without prestressing force, a significant curvature can be reached. For increasing values of the prestressing force up to the limiting value of 130 kN, there is a steady increase in the curvature, ranging from 0.065 m^{-1} to 0.09 m^{-1} (38%), whereas the bending moment increases substantially from 1 kN m to 2.75 kN m. The efficiency of the prestress is limited in terms of achieving larger activation curvatures, but pays off when considering the increase of cross-sectional strength. Finally, the larger the prestress force, the smaller the ratio between ultimate bending moment and bending moment at a UHPFRC strain of 0.002: with no prestress, the ratio in the analysed cross-section is about 2.1, and it falls to 1.5 for the limiting value of the prestress force.

3. Design of the experimental footbridge

3.1. Concept

The structural system of the experimental footbridge bases on the

Fig. 8. Small-scale GFRP footbridge prototype using the bending-active bow-string concept [23].

bending-active bow-string concept as devised by Joseph Paxton for the so-called *Paxton gutters*, extensively used in the construction of the Crystal Palace [21]: a slender beam is bent by the action of a lower rod in tension and one or more deviators. In the case of Paxton's gutters, the beam was made of timber and served as gutter and as carrying member for the glazed roof, and the induced curvature was beneficial for both functions. Compared with a similar system with no curvature in the beam, the structural function is enhanced because the induced curvature opposes the one caused by gravity loads on the beam. Our group has successfully tested the bending-active bow-string concept with a laboratory prototype made of GFRP rods as pre-bent members, timber deviators, steel connections and steel-wire cables [23] (Fig. 8). Tests on the GFRP prototype showed that the structure was very flexible. It was natural to investigate a similar concept using UHPFRC, which would provide a more rigid structure.

The UHPFRC concept consists of (a) a prestressed monolithic UHPFRC slender deck; (b) a deviator located at mid-span; (c) activation cables attached to both ends of the deck and to the bottom of the deviator. As discussed in Sect. 2.4, the strength and the activation curvature of the UHPFRC deck can be controlled by introducing prestress in the deck cross-section. The proposed production process is as follows (Fig. 9): 1. The UHPFRC deck is casted on a flat surface including the necessary centred tensioned pre-stressing strands; 2. Pre-stress is

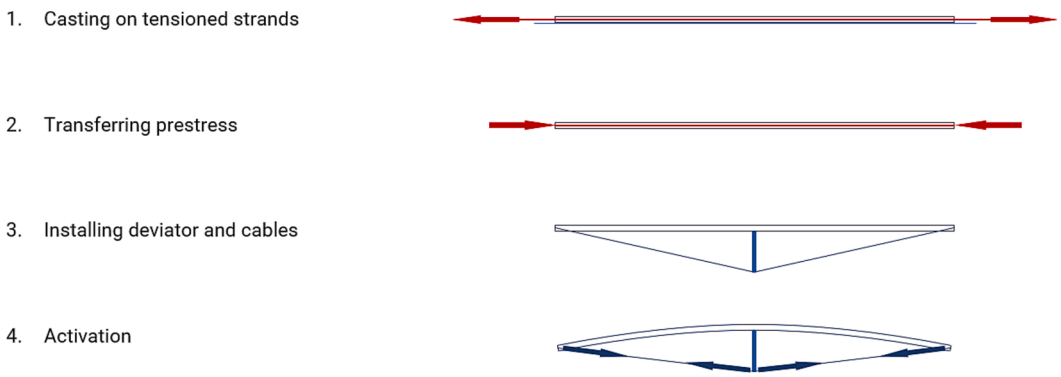

Fig. 9. Conceptual production process of an UHPFRC footbridge [16].

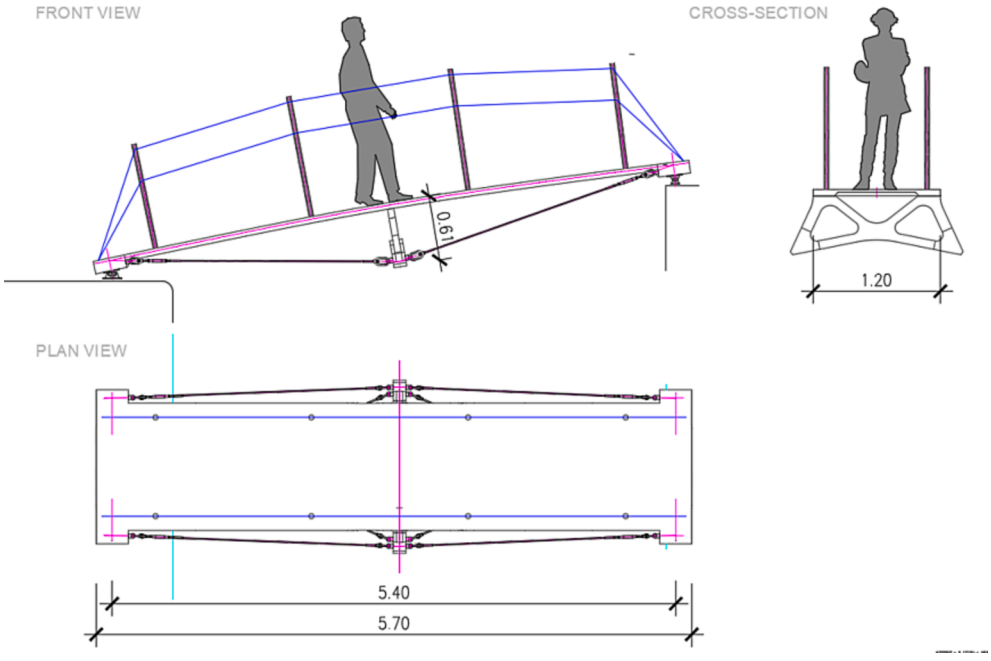

Fig. 10. Front view, plan view and cross-section of the experimental footbridge. Dimensions in m.

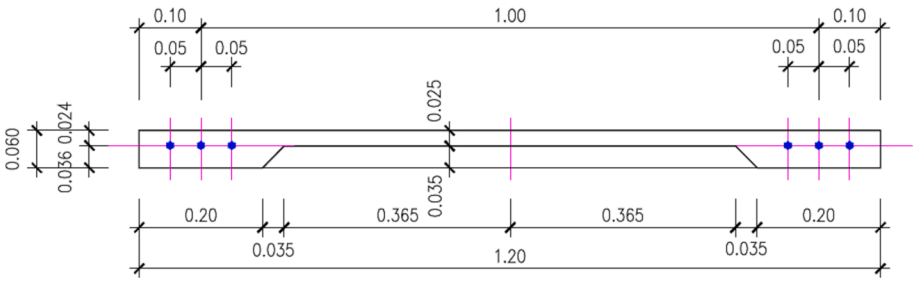

Fig. 11. Typical cross section of the footbridge. Dimensions in m.

Table 1
Gross section properties for the deck frame elements.

A (m^2)	d_G (m)	I_y (m^4)	I_z (m^4)	J (m^4)
40.74×10^{-3}	24.0×10^{-3}	4.72×10^{-3}	11.195×10^{-6}	26.15×10^{-6}

transferred to the deck; 3. Deviators and external cables are installed; 4. The deck is pre-bent by introducing forces in the external cables.

3.2. Description of the structure

In the fall of 2020, the opportunity to test the bending-active bow-string footbridge concept using an UHPFRC active deck arose. A small footbridge to span the gap between the wharf and an experimental structure located in the dock of Sagunto's Port (Spain) was needed. A 5.4 m span bending-active structure with an active deck and a single central deviator was designed (Fig. 10). The bending-active deck is 0.06 m thick, 5.7 m long and 1.2 m wide, made of UHPFRC with f_{cm}=150 MPa. It has 1.45 m wide end transverse beams to accommodate the footbridge supports as well as the anchorages for the external cables. The truss shaped UHPFRC central deviator has the same material specification as the deck and is 0.55 m high. The external cables are anchored to the bottom corners, and the width of the bottom part is 1.63 m. With this arrangement the main external cables are contained in inclined planes and provide increased torsional stiffness to the structure. The cable system is made of (a) four external AISI 316 stainless steel main cables (1×19Ø10) and (b) 2+2 X-bracing cables (1×19Ø8) of the same material. The footbridge rests on two AISI 316 hinged supports on the dock side and two sliding supports of the same material on the wharf side.

3.3. Cross-section design

The 150 MPa UHPFRC cross-section of the deck is monolithic and is represented in Fig. 11. It has a maximum depth of 6 cm to accommodate the prestressing strands, arranged in two groups of three units at each side, and to provide the needed flexibility for the bending activation. The thickness of the central part amounts to 2.5 cm to reduce the UHPFRC material consumption and the weight of the structure. The strands (3+3 Y1860 S7 0.5″ units) are located along the neutral axis of the cross-section. Their arrangement provides sufficient cover and separation to ensure a proper distribution of fresh UHPFRC during placement. The deck is designed to be casted on a flat formwork, pre-stressed and then pre-deformed to achieve the target curved shape.

Moment-curvature diagrams for several values of the prestressing force prior to transfer have been computed according to the method of Sect. 2.3 to find the limiting value of the force which is the one that corresponds to ultimate compressive and tensile strains in the top/bottom fibres. For that purpose, a reduced width equal to 1.02 m –by detracting 0.18 m of the central part– has been adopted to account for shear lag; the resulting gross sectional properties are listed in Table 1.

According to the activation concept shown in Fig. 9, the section will

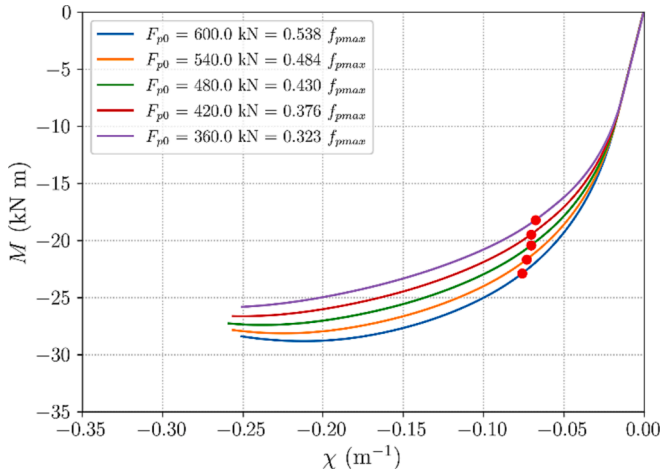

Fig. 12. Negative moment–curvature diagrams of the experimental footbridge cross-section for different values of the prestressing force. Red dots correspond to a 0.002 tensile strain in UHPFRC. The green curve corresponds to the limiting prestressing force (6×80 kN). (For interpretation of the references to colour in this figure legend, the reader is referred to the web version of this article.)

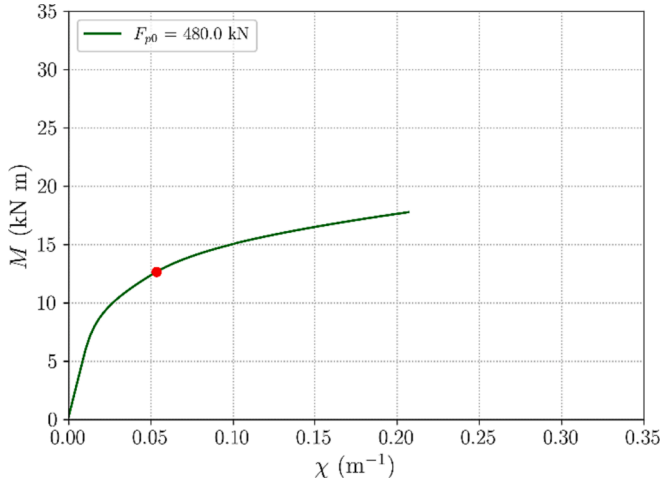

Fig. 13. Positive moment–curvature diagrams of the experimental footbridge cross-for a prestressing force of 6×80 kN.

be under the action of negative bending moments. By analysing the moment–curvature diagrams for several values of the prestressing force (see Fig. 11) with the method explained in Sect. 2.3, it has been found that the limiting force is 480 kN (80 kN in each tendon). Considering the experimental nature of the footbridge, it was decided to reach this limiting value of the prestress in order to allow for a large curvature in

Table 2
Simplified moment–curvature diagram for the model plastic hinges.

M (kN m)	−27.27	−7.68	−3.57	−1.8	0	6.02	9.58	13.24	17.77
χ (m^{-1})	−0.25	−0.0704	−0.0327	−0.0165	0	0.0104	0.0239	0.0615	0.21

Table 3
Section dimensions for frame and cable elements.

	End transverse beams	Central transverse beam	Deviator external frame	Deviator internal frames
b (m)	0.30	0.30	0.06	0.06
h (m)	0.10	0.06	0.10	0.08
	Main cables (1×19Ø10)	Bracing cables (1×19Ø8)		
A (mm^2)	59	38		

Table 4
Material properties for the frame sections.

Material	γ (kN/m^3)	E (MPa)	ν	α (C^{-1})
UHPFRC	25	50 000	0.2	1.0×10^{-5}
AISI 316 cables	75	125 000	0.3	1.6×10^{-5}

the activation phase. The behaviour under negative moments is depicted by the green curve in Fig. 12. The corresponding positive moment–curvature diagram is represented in Fig. 13. The lower performance for positive moments is not a problem because the deck is mainly subjected to negative ones.

3.4. Structural model and activation protocol

The analysis has been carried out with SAP2000™ v21 implementing a 3D frame element model. The deck has been modelled with 0.1 m long elements with section properties listed in Table 1 (see Sect. 3.3). At the centre of each deck frame element a 0.05 m long plastic hinge to model the non-linear behaviour of the deck cross-section has been defined; the moment–curvature diagram for the hinge is a simplification from the one calculated in Sect. 3.3 and is displayed in Table 2. The deck is joined to the end and central transverse beams, and the deviator frame elements are joined to the end of the central transverse beam; these elements have been modelled with rectangular cross-sections. Each cable segment has been modelled with two elements with equivalent circular cross-section; flexural rotations have been released at the end joints of each cable. The section dimensions for the elements are included in Table 3, and the properties of the materials are displayed in Table 4. The structure has a pinned support and a transverse direction sliding support at one side, and free sliding supports at the other side. The 3D frame model is shown in Fig. 14.

The activation process has been simulated by means of a P-Delta staged analysis with large displacements, and the sequence described in Fig. 15. The stages in which the structure was positioned upside-down have been modelled in the upright position with gravity pointing upwards; however, the images of the model in Fig. 15 have been turned over to match the real orientation of the structure at each stage.

The maximum negative moment at the deck mid-span section is found at stage 2 of the activation process, in which the activation load is applied. It is modelled as a point load acting vertically on the deviator to produce the bending of the deck. The activation is a short-term temporary process in which the deflections are being controlled. In addition, the direction in which self-weight acts is the opposite as in the final, upside-down, position. For these reasons, a reduced partial factor of 1.05 for the self-weight and for the activation load has been considered appropriate to check the deck during the activation. Table 5 contains the relevant design internal forces for the mid-span section. Note that for the maximum negative bending moment in stage 2 the ratio between the ultimate and the design moment is $M_{ultimate}/M_d$=−27.27/(−17.43)= 1.565 (see Fig. 12 and Table 2 for the value of $M_{ultimate}$), which is considered a sufficient security factor for the construction stage.

In addition to modelling the activation process, the structure has been checked according to Eurocodes. Apart from the dead loads, the variable actions included in Table 6 have been considered.

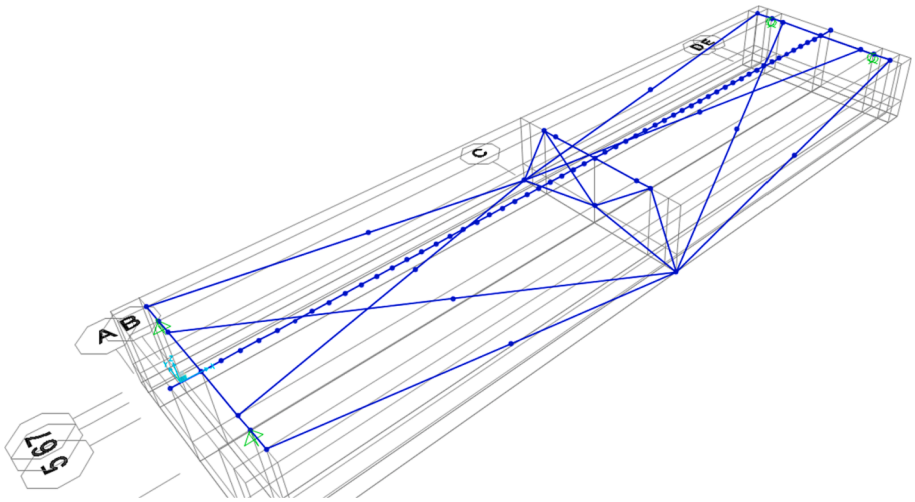

Fig. 14. 3D frame element model of the structure.

1. After casting the prestressed deck and the deviator in upside down position, the structure is placed on temporary supports. Estimated mid-span deflection: 26 mm

2. The deck is loaded on the midspan section to reach a target deflection od 104 mm. Estimated *activation load*: 9.425 kN

3. Installation of the main cables (Ø10 mm) and unloading of 2/3 of the activation load. Target mid-span deflection: 91 mm.

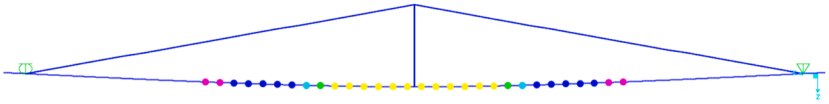

4. Installation of the X-bracing cables (Ø8 mm) and unloading of the remaining activation load. Target mid-span deflection: 86 mm.

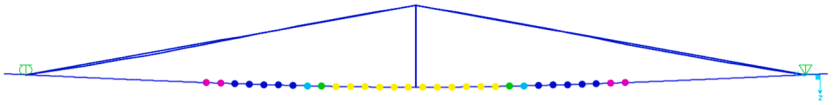

5. The structure is turned over to the upright position. Target mid-span deflection: 75 mm.

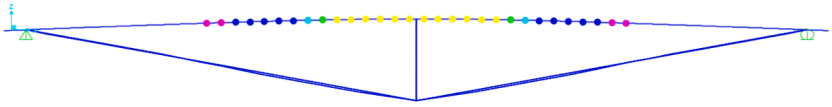

Fig. 15. Modelling of the activation process. Coloured dots show the activation of the plastic hinges.

Table 5
Design internal forces during the activation.

Relevant stage	Cross-section	N_d (kN)	V_d (kN)	M_d (kN m)
2. Maximum deflection	Mid-span	0	4.87	−17.43
5. End of the activation process	Mid-span	−31.66	5.24	−12.56

The relevant load combinations for checking the ultimate limit states (ULS) are:

$$\text{LC1}: \ 1.35\ \text{G} + 1.35\ \text{P}_2 + 1.35\ \text{Q} + 0.3{\cdot}1.5\ \text{W} + 0.6{\cdot}1.5\ \Delta\text{T}_{\text{con}}, \tag{10.a}$$

$$\text{LC2}: \ 1.05\ \text{G} + 0.95\ \text{P}_2 + 1.35\ \text{SHR} + 1.35\ \text{QS}_1 + 0.3{\cdot}1.5\ \text{W} + 0.6{\cdot}1.5\ \Delta\text{T}_{\text{exp}}, \tag{10.b}$$

where G are the permanent loads, P_2 is the activation load, Q is the live load on the whole deck, QS_1 is the live load on a single half of the deck, W is the wind load, SHR is the shrinkage, ΔT_{con} is the thermal contraction and ΔT_{exp} the thermal expansion. The combination LC1 produces the maximum negative moment at the mid-span section after the construction stage, and LC2 causes the maximum positive moment at the section located at a distance of 0.9 m from the support, and the maximum shear force at the mid-span section. The values of the internal

Table 6
Variable actions.

Action	Basic value		Value on model
Live load	5.00 kN/m^2		4.50 kN/m
Wind pressure	0.976 kN/m^2	Lateral wind load	0.634 kN/m
		Vertical wind load	±1.054 kN/m
Thermal action	Deck	expansion	+26 °C
		contraction	−17 °C
	Cables	expansion	+46 °C
		contraction	−27 °C
Shrinkage			-0.7×10^{-3} m/m

Table 7
Design internal forces after the activation.

ULS (load case)	Cross-section	N_d (kN)	V_d (kN)	M_d (kN m)
Max. negative moment (LC1)	Mid-span	−78.92	12.79	**−13.81**
Max. positive moment (LC2)	0.9 m from supp.	−50.03	0	**3.02**
Max. shear force (LC2)	Mid-span	−49.94	**13.42**	−9.64

forces are given in Table 7. None of the forces after the activation is critical for the design.

The relevant load combination for the serviceability limit state of deflections is:

$$\text{LC3}: \ G + P_2 + 0.4\ Q, \tag{11}$$

where the frequent fraction of the live load has been used. The active vertical deflection for this load combination is 0.007 m, which corresponds to 1/760 of the span length, and is considered acceptable for this experimental structure. Finally, the vibration modes have been analysed. The first 16 modes correspond to cable vibrations. The first mode of the deck is a global torsional one with a frequency of 89.2 Hz, and the second one is a global flexural mode with one semi-wave and a frequency of 100.6 Hz. Both are far from the critical range of frequencies for footbridges.

4. Production

4.1. UHPFRC characterization

The UHPFRC for the deck and the deviator was produced at the

Fig. 16. Casting of the deviator. Left: formwork and minimum reinforcement; right: the deviator after unmoulding.

Fig. 17. Casting of the deck. Upper-left: formwork table and prestressing tendons and devices; upper- right: countermould prepared above the formwork and positioned deviator; lower row: two images of the casting process.

Fig. 18. Activation process. Upper-left: the structure after unmoulding (the external cables bear no tension); upper- right: the structure resting on lateral supports made of wooden blocks, loaded in the centre (note the slack cables); lower-left: external cables have been shortened in preparation for the first unloading step; lower-right: pre-deformed structure with cables in tension after full removal of the activation load.

laboratory of ICITECH (Universitat Politècnica de València). It has a fibre content of 160 kg/m^3 of smooth-straight (13/0.20) steel fibres. It is characterized by a mean compressive strength f_{cm}=155 MPa, a mean tensile strength f_{ctfm}=9 MPa, an equivalent strain $\varepsilon_{ct2}=2\times10^{-3}$, which marks the maximum fibre efficiency, a peak tensile strength corresponding to ε_{ct2} equal to 10 MPa, an equivalent strain at failure $\varepsilon_{ct3}=10\times10^{-3}$, and Young's modulus E=53000 MPa. The tensile properties have been determined using a simplified inverse analysis method proposed by the authors, based on four-point bending tests on 100 mm × 100 mm × 500 mm specimens. This method is described in detail in Ref. [1].

4.2. Casting of the deviator

The first element to be produced was the deviator. It was cast on a formwork table with the help of a countermould. Minimal reinforcement and a constructive connection can be observed in Fig. 16.

4.3. Casting and prestressing of the deck

The deck was cast in upside-down position on a formwork table. A countermould was prepared above the table to be pressed on the fresh concrete right after pouring it (Fig. 17); with it, the proper shape of the bottom face of the deck was achieved. The six prestressing tendons were tensioned with an initial force of 80 kN each one as explained in Sect. 3.3. The deviator was positioned in place before the pouring begun. The prestressing force was transferred after 72 h.

4.4. Activation process

After removing the moulds, the deck was separated from the formwork table, lifted with a crane and left to rest on wooden supports. The external cables were installed without tension, and the target shape was provided by loading the central part with steel bars to reach the initial deflection of 104 mm (step 2 of the process described in Fig. 15). After that, the external cables were tightened to make them taut, and part of the load was removed (step 3, Fig. 15). Then, the X-bracing cables were tightened, and the remaining load was removed (step 4, Fig. 15). Images of this process are included in Fig. 18.

Table 8
Applied load and mid-span deflection during the activation process.

Activation load (N)	0	3400	**6800**	3400	0
Measured deflection (mm)	80	95	105	102.5	101
Planned deflection (mm)	24	–	104	86	75

The measured loads and mid-span deflections during the activation process are included in Table 8. There are several remarkable aspects in the measurements: with no additional load, the initial midspan deflection was 80 mm, much larger than the expected 24 mm. This was due to the need to forcefully pull the deck to separate it from the formwork table, that caused remnant deformation of the deck. As a consequence, the target deflection of 104 mm was reached with less load than foreseen (compare with step 2 in Fig. 15), and the remnant deflection after the activation load was fully removed was also larger than foreseen (101 mm vs. 75 mm). The activation process and the consequences for the geometry of the structure are further discussed in Sects. 4.6. and 5.2. Fig. 19 shows the turning manoeuvre with the crane and Fig. 20, the footbridge resting in the upright position ready for being tested.

The tension in the cables was adjusted by measuring their individual vibration frequency after turning over the footbridge, to achieve similar forces among all external cables and among the X-bracing cables.

4.5. Installation in Sagunto Port

The structure was transported to Sagunto Port and installed on a

Fig. 19. Turning the structure into the upright position. (Coloured sheets provided a rough texture to the deck surface.).

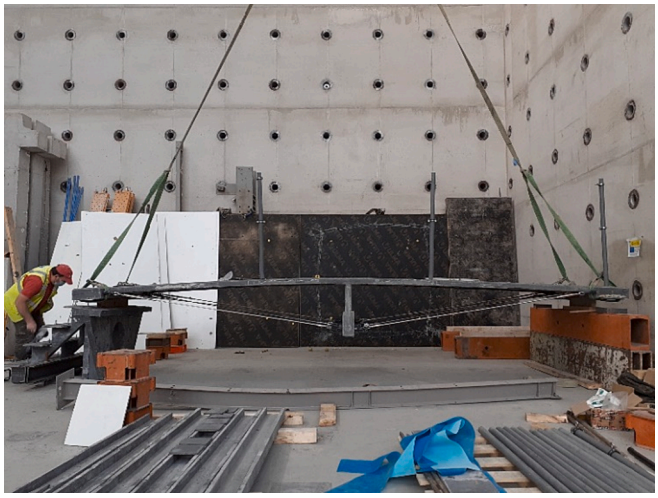

Fig. 20. The footbridge before being tested.

Fig. 22. Localized defects in the bottom face of the deck.

Fig. 21. The footbridge in the final location. The image on the right shows the finished cable handrails as well as a non-structural lateral baseboards. The cable anchored to the wharf at the forefront is securing the block on the water and is not attached to the footbridge.

Fig. 23. Smeared cracks along the upper face of the deck. Left: concentrated cracks at the localized weaker cross-section; right: smeared cracking pattern along the upper face of the deck.

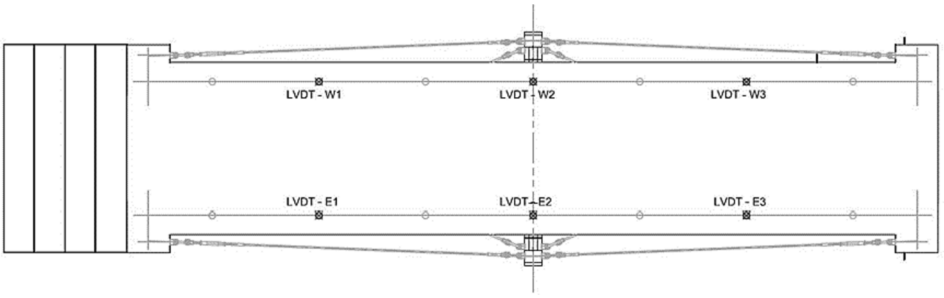

Fig. 24. Position of the vertical displacement transducers.

wharf to give access to a temporary testing structure in December 2020. Fig. 21 shows two images of the structure.

4.6. Discussion

The most critical part of the construction process was the pouring of UHPFRC and the unmoulding of the deck. Two problems arose: firstly, two small localized areas at the inner corners of the longitudinal girders were not completely filled (see Fig. 22) as a consequence of the use of the countermould, which was pressed on the fresh UHPFRC, creating a localized weak deck cross-section near the deviator; secondly, due to the bolts that were required to position the railing posts' fixations, it was necessary to forcefully pull the deck upwards to detach it from the formwork table. This caused premature cracking of the deck which concentrated at the weak cross-section (Fig. 23, left), a larger-as-planned deformation after the activation, and partly disrupted the planned activation process as shown in Table 5. The existence of a weaker section and the detachment from the formwork table had a geometric consequence after the activation, which is analysed in Sect. 5.2. The cracking pattern along the upper face of the deck, apart from the described localized problem, was smeared and sufficiently uniform (Fig. 23, right): the type of cracking was basically microcracking and, in a visual inspection, the observed crack width did not reach 0.05 mm.

5. Testing

5.1. Load test

After the activation process, and prior to the installation in Sagunto Port, a load test was carried out at the laboratory. The footbridge was placed horizontal and rested on simple supports (Fig. 20). Six vertical displacement transductors, marked as LVDT in Fig. 24, were used to measure deformations; they were located in pairs at the mid-span and quarter-span sections. Six load models were tested: two symmetrical modes with half load (1.57 kN/m) and full load (2.94 kN/m), two asymmetrical modes with full load on the north and on the south half of the deck, and two torsional modes with full load on the east and on the west half of the deck. The load was introduced using 25 kg cement bags stacked in two layers: a bottom layer with a maximum of 2×16 bags (8 kN) and a top layer with 2×14 bags (7 kN). Fig. 25 shows the six load arrangements.

The displacements measured in the load tests have been compared with model results extrapolated to the location of the transducers. Results are shown in Table 9. Both measured and model displacements are in reasonable agreement, with the larger differences appearing in the torsional modes.

5.2. Geometric control

Right after the load test, a first qualitative control of the geometry was carried out by comparing the theoretical profile of the upper face of the deck with the profile obtained from a frontal photograph. The result

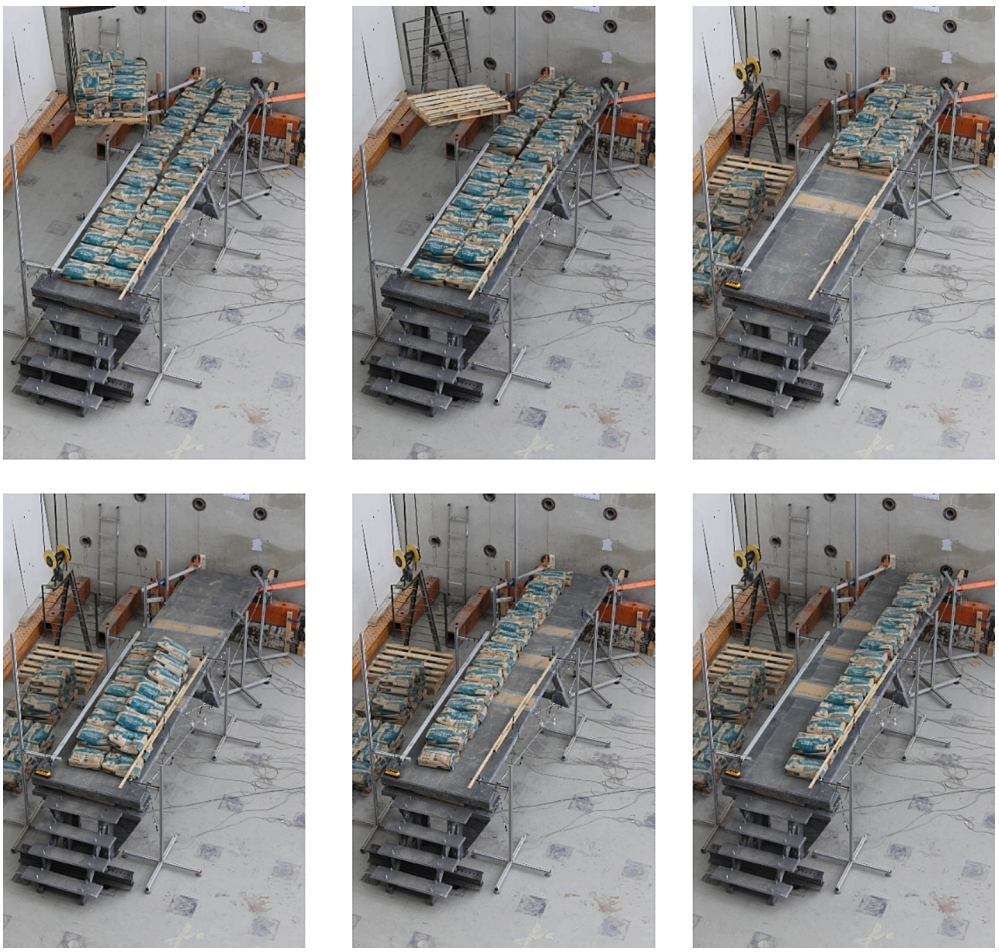

Fig. 25. Load modes. From left to right and top to bottom: Symmetric 1 (1.57 kN/m); Symmetric 2 (2.94 kN/m); Asymmetric N; Asymmetric S; Torsional W; Torsional E.

Table 9
Measured displacements in the load test vs. model results. All displacements in mm.

	Symmetric 1		Symmetric 2		Asymmetric N		Asymmetric S		Torsional W		Torsional E	
LVDT	Model	Test	Model	Test	Model	Test	Model	Test	Model	Test	Model	Test
W1	5.2	3.9	10.3	8.1	3.4	3.2	7.0	6.1	6.6	4.9	3.8	4.3
W2	6.4	5.6	12.8	11.8	6.4	6.1	6.4	6.2	8.0	6.6	4.8	5.6
W3	5.2	4.6	10.3	9.3	7.0	6.7	3.4	4.1	6.6	5.8	3.8	4.9
E1	5.2	4.5	10.3	9.2	3.4	3.6	7.0	4.7	3.8	4.6	6.6	7.8
E2	6.4	6.2	12.8	12.3	6.4	6.7	6.4	7.2	4.8	6.3	8.0	8.4
E3	5.2	4.5	10.3	8.9	7.0	6.4	3.4	3.9	3.8	4.8	6.6	5.5

is merely qualitative, because the photograph has distortional errors due to the projection, but it provides a first impression of the discrepancy between the design and the realized structure. This initial assessment shows remarkable differences in the vertical direction in the left span after the activation, with maximum values on the order of 2 cm as shown in Fig. 26.

In order to have an accurate estimation of the final geometry, a laser scan of the geometry was carried out in December 2021, one year after the placement of the footbridge in Sagunto port. Terrestrial laser scanners are instruments that can measure three-dimensional (3D) coordinates of objects at high-speed using a laser, resulting in high-density 3D point cloud data [24]. Laser scanning technology is especially valuable to reconstruct objects digitally, and especially when the geometry of the object is complex, and the size of its surface is large [25]. This 3D survey, used successfully in numerous areas of civil engineering, allows obtaining a digital model of the object with a high level of detail.

To obtain the 3D model of the surface of the footbridge, a Leica RTC360 laser scanner was used. The scan was performed from 9 positions obtaining a complete point cloud formed by 91,707,989 points. After processing and adjusting the point clouds, a 3D model of the footbridge has been recorded in millimetre detail. The result of the scan offers us the reverse engineering of the structure, since once it is built, it is possible to compare the theoretical design with the 3D model at real scale. Fig. 27 shows two views of the obtained 3D point cloud.

Averaged points along the longitudinal centreline of the upper face have been extracted from the 3D point data cloud. Centreline points have been inferred by displacing the upper face points 24 mm downwards (refer to Table 1). From these data, a 6th degree polynomial has been fitted using least-squares minimization; it represents the centreline curve in the installed structure. The result is shown in Fig. 28, where the planned centreline from the FE model after the activation process has been also included.

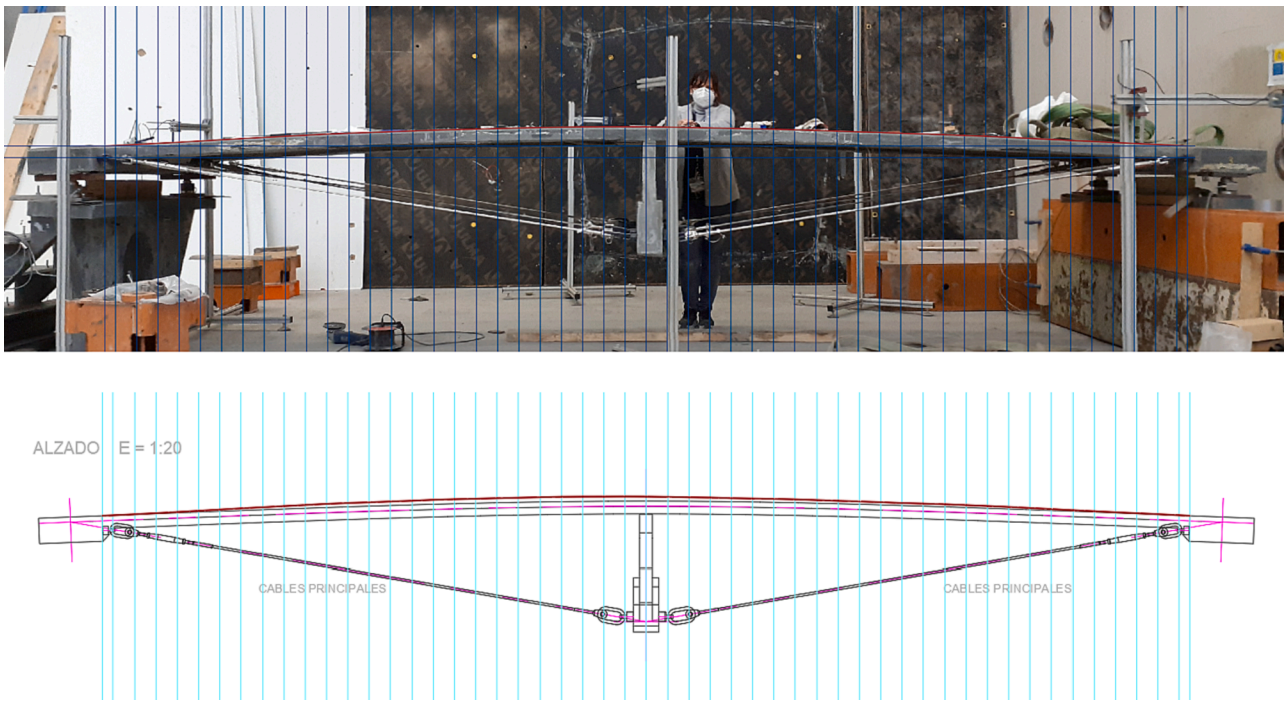

Fig. 26. Qualitative assessment of the geometry of the deck after the activation. The red line, representing the top surface, has been drawn on a photograph of the built structure (top image) and translated to the design front view (bottom image, grey colour). Differences of 2 cm are visible in the left part. (For interpretation of the references to colour in this figure legend, the reader is referred to the web version of this article.)

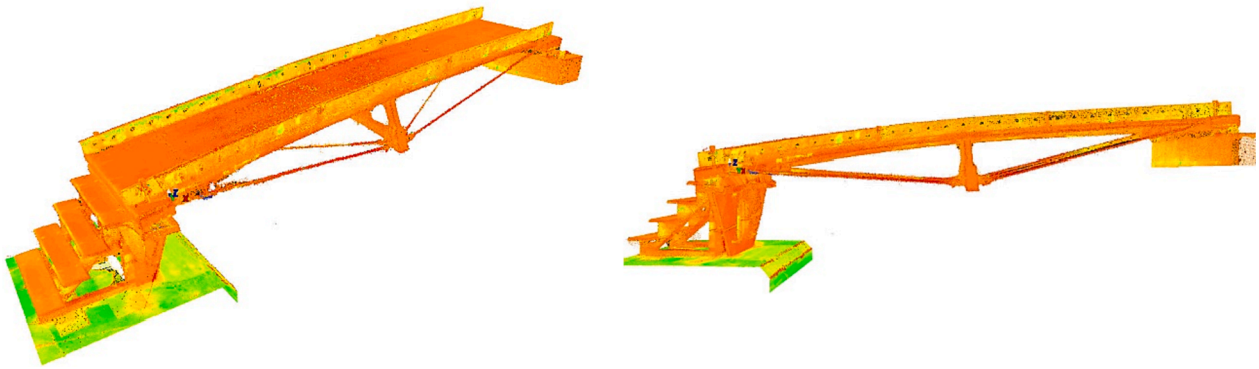

Fig. 27. Two views of the 3D point cloud resulting from the laser scan of the finished footbridge.

The survey data confirm the qualitative assessment of Fig. 26. The real activation process caused a larger deformation as foreseen: about 2 cm in the central part of the deck. The existence of a weaker section (see Sect. 4.6) explains the non-symmetrical deformed centreline, in which the maximum deformation is located on the left of the mid-span cross-section.

The curvature of the centreline can be straightforwardly calculated from the fitted centreline polynomial as $\chi = y''/(1+y'^2)^{3/2}$. Fig. 29 reflects the result of this calculation (red curve) compared to the curvature extracted from the SAP2000 analysis model (light blue curve). As expected after the analysis of the survey data, the extremal value (-0.041 m^{-1}) is 28 % larger than the one from the model (-0.032 m^{-1}) and it is shifted to the left of the mid-span section. Note that the values near both ends of the structure have been omitted because curvatures of the fitted polynomial are not representative in these regions. Despite the larger values, the magnitude of the curvatures is still in the linear and quasi-linear range of the moment–curvature diagram of the cross-section (see Fig. 12, green curve) and the peak UHPFRC tensile stress (red dot in Fig. 12) is not reached.

6. Conclusions

This paper presents the design-to-production process of an experimental 5.4 m span bending-active footbridge consisting of an upper UHPFRC pre-bent slender deck, a lower stainless steel cable system and an intermediate UHPFRC deviator. The deck was cast as a flat prestressed slab, bent to the target shape, and stabilized with the external cables. UHPFRC on the boundary between strain hardening and softening has been used. The research focuses on the specificities of pre-bending slender prestressed UHPFRC cross-sections. The main conclusions are:

1. An algorithm to estimate moment–curvature diagrams of prestressed UHPFRC cross-sections has been developed and applied to a rectangular test section for different values of the prestressing force. The UHPFRC material model reproduces the behaviour of the UHPFRC produced in the laboratory, on the boundary between strain hardening and softening. The numerical results show that (a) significant curvatures can be reached within the range of efficiency of the fibres,

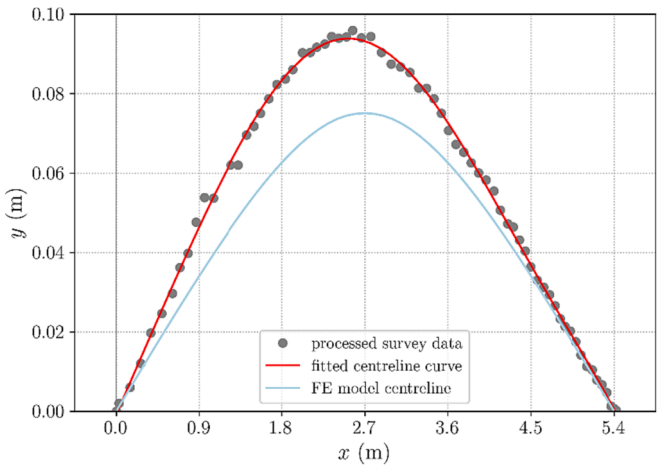

Fig. 28. Centreline points extracted from survey data (grey points), fitted centreline curve (red), and estimated centreline after activation according to the FE model (light blue). (For interpretation of the references to colour in this figure legend, the reader is referred to the web version of this article.)

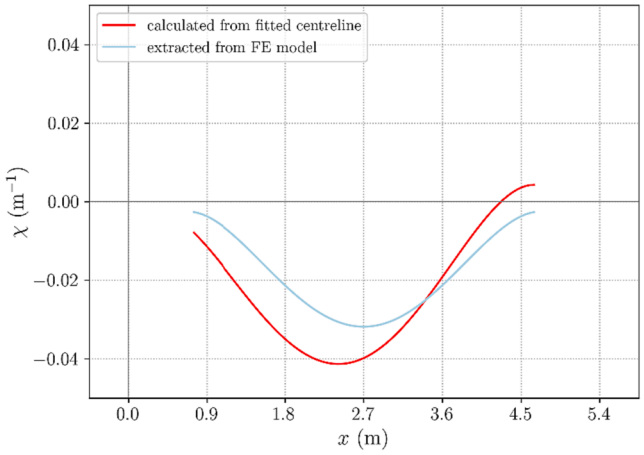

Fig. 29. Curvature diagram of the centreline: calculated from the fitted centreline from survey data (red); extracted from the SAP2000 analysis model (light blue). (For interpretation of the references to colour in this figure legend, the reader is referred to the web version of this article.)

even with no prestressing force; (b) the curvature that the section can reach within the efficiency range of the fibres increases for larger prestressing forces; and (c) the resisted bending moment substantially increases for larger prestressing forces.

2. Based on the described section model and algorithm, slender prestressed UHPFRC members made of UHPFRC on the boundary between strain hardening and softening can reach curvatures that allow their use in bending-active structures.
3. The activation of the footbridge prototype and its service and ultimate limit states have been analysed by means of a staged FE model with the sectional behaviour computed with the previously referred algorithm. The results of the analysis show that the highest internal forces in the deck are found during the bending activation phase, and all design combinations result in less critical forces. The structural deformation in service states is sufficiently small and the eigenfrequencies of the structure are well above the critical range.
4. The footbridge prototype has been built and tested in the laboratory. Load test results show good agreement with the FE model.
5. The geometry of the finished structure has been surveyed by means of a terrestrial laser scanner. The analysis of the geometry shows that the initial bending activation of the real structure produced 20% larger deformations than the planned ones due to the UHPFRC casting and unmoulding process. Despite this fact, the equivalent UHPFRC tensile strain of 0.002 was not reached for the curvatures of the deck inferred from survey data, and the cross-section behaviour remained in the linear or quasi-linear range.
6. Even for the larger than planned deflections during activation, the observed cracking pattern of the deck consisted of microcracks with width below 0.05 mm. This is consistent with the fact that the equivalent UHPFRC tensile strain was below 0.002, still within the efficiency range of the fibres.
7. The results of the experiment show that the design of the mould, the UHPFRC casting, and the bending activation phase are critical stages of the process. Further research will be aimed at achieving a more controllable and reliable activation of the UHPFRC structural members. Further research is also needed to analyse and verify expected structural failure modes.

In summary, this article shows the design and production of a lightweight type of footbridge, with a novel use of UHPFRC as pre-bent structural element, with a straightforward design procedure, and involving a very low amount of material resources. It is a promising step towards building larger span structures of this kind.

CRediT authorship contribution statement

Carlos Lázaro: Conceptualization, Software, Formal analysis, Writing – original draft, Writing – review & editing, Supervision. **Carmen Castro-Bugallo:** Methodology, Resources, Investigation, Data curation. **Juan Navarro-Gregori:** Methodology, Writing – review & editing. **Enrique Priego-de-los-Santos:** Investigation, Visualization. **Pedro Serna:** Writing – review & editing, Resources, Funding acquisition.

Declaration of Competing Interest

The authors declare that they have no known competing financial interests or personal relationships that could have appeared to influence the work reported in this paper.

Data availability

Data will be made available on request.

Acknowledgements

The authors are grateful to Rover Maritime for facilitating the placement of the footbridge as access to their prototype in the H2020 *Reshealience* project.

References

[1] Mezquida-Alcaraz EJ, Navarro-Gregori J, Serna-Ros P. Direct procedure to characterize the tensile constitutive behavior of strain-softening and strain-hardening UHPFRC. Cem Concr Compos 2021;115:103854.
[2] Lopez JA, Serna P, Camacho E, Coll H, Navarro-Gregori J. First ultra-high-performance fibre-reinforced concrete footbridge in Spain: Design and construction. Struct Eng Int: J Int Assoc Bridge Struct Eng (IABSE) 2014;24:101–4.
[3] Happold E, Liddell W. Timber Lattice Roof for the Mannheim Bundesgartenschau. Struct Eng 1975;53:99–135.
[4] Du Peloux L, Tayeb F, Baverel O, Caron JF. Construction of a Large Composite Gridshell Structure: A Lightweight Structure Made with Pultruded Glass Fibre Reinforced Polymer Tubes. Struct Eng Int 2016;26:160–7.
[5] Lienhard J, Alpermann H, Gengnagel C, Knippers J. Active Bending, a Review on Structures where Bending is used as a Self-Formation Process. Int J Space Struct 2013;28:187–96.
[6] Baverel O, Caron JF, Beaugelin M, Bonthoux J, Martin S. Concept of a Beam Prestressed by Bending: Application to a Footbridge in Composite Materials. J Int Assoc Shell Spatial Struct 2010;51:99–106.
[7] Bessini J, Piñol R, Lázaro C, Monleón S. Design of an experimental lightweight footbridge based on the active bending principle. In: Mueller C, Adriaenssens S,

editors. Creativity in Structural Design. Proceedings of the IASS Symposium 2018, Boston; 2018.
[8] Bessini J, Lázaro C, Casanova J, Monleón S. Efficiency-based Design of Bending-active Tied Arches. Eng Struct 2019;200:109681.
[9] Bessini J, Shepherd P, Monleón S, Lázaro C. Design of bending-active tied arches by using a multi-objective optimization method. Structures 2020;27:2319–28.
[10] Kotelnikova-Weiler N, Douthe C, Lafuente-Hernandez E, Baverel O, Gengnagel C, Caron JF. Materials for Actively-Bent Structures. Int J Space Struct 2013;28:229–40.
[11] Ashby MF. Materials Selection in Mechanical Design. 4th ed. Butterworth-Heinemann; 2011.
[12] McLean W. Building with Air: The Pneumatically Powered Construction Systems of Dante Bini. In: Cambpbell JWP, Bill N, Driver M, Heaton M, Pan Y, Tutton M *et al.*, editors. Further Studies in the History of Construction. Proceedings of the Third Annual Construction History Society Conference, Cambridge; 2016.
[13] Kromoser B, Kollegger J. Pneumatic forming of hardened concrete - building shells in the 21st century. Struct Concr 2015;16:161–71.
[14] Ochs F, Lichtenfels A, Koch H, Heidemann W, Müller-Steinhagen H. Heißwasser-Erdbecken-Wärmespeicher mit freitragender Abdeckung für solare Nahwärmesysteme. In 17. Symposium Thermische Solarenergie, Bad Staffelstein; 2007.
[15] Khorami M, Navarro-Gregori J, Serna P. Serviceability behaviour of reinforced UHPFRC tensile elements: Assessment of the ratio between maximum and average crack widths. Constr Build Mater 2021;303:1–14.
[16] Lázaro C, Castro-Bugallo C, Navarro-Gregori J, Serna P. Exploring concepts for UHPFRC bending-active footbridges. In: Footbridge, Madrid; 2022.
[17] Russell HG, Graybeal BA. Ultra-High Performance Concrete: A State-of-the-Art Report for the Bridge Community. Federal Highway Administration - U.S. Department of Transportation; 2013.
[18] Lienhard J. Bending-Active Structures: Form-Finding Strategies using Elastic Deformation in Static and Kinetic Systems and the Structural Potentials therein. Institut für Tragkonstruktionen und Konstruktives Entwerfen (ITKE), Universität Stuttgart; 2014.
[19] Resplendino J, Baby F, Baroghel-Bouny V, Behloul M, Brisard S, Carcasses M *et al.* Ultra High Performance Fibre-Reinforced Concretes; Recommendations. Revised edition, June 2013. Groupe de travail BFUP, Association Française de Génie Civil; 2013.
[20] Leutbecher T, Fehling E. Tensile behavior of ultra-high-performance concrete reinforced with reinforcing bars and fibers: minimizing fiber content. ACI Struct J 2012;109:253–63.
[21] Addis B. The Crystal Palace and its Place in Structural History. Int J Space Struct 2006;21:3–19.
[22] Comisión Permanente del Hormigón. Instrucción de Hormigón Estructural (EHE-08). Madrid: Centro de Publicaciones del Ministerio de Fomento. Gobierno de España; 2008.
[23] Bessini J. Form-finding and performance of bending-active structures. Proposals of application to lightweight braced arches. Universitat Politècnica de València; 2021. Doctoral dissertation.
[24] Rachakonda P, Muralikrishnan B, Cournoyer L, Sawyer D. Software to Determine Sphere Center from Terrestrial Laser Scanner Data per ASTM Standard E3125–17. J Res Nat Inst Stand Technol 2018;123:123006.
[25] Lee IS, Lee OL, Park HJ, Bae KH. Investigations into the influence of object characteristics on the quality of terrestrial laser scanner data. J Civ Eng 2010;14:905–13.